



ARCHIVE

Label-Free Nanoplasmonic-Based Short Noncoding RNA Sensing at Attomolar Concentrations Allows for Quantitative and Highly Specific Assay of MicroRNA-10b in Biological Fluids and Circulating Exosomes

Gayatri K. Joshi,[†] Samantha Deitz-McElvea,[‡] Thakshila Liyanage,[†] Katie Lawrence,[†] Sonali Mali,[†] Rajesh Sardar,^{*,†,§} and Murray Korc^{*,‡}

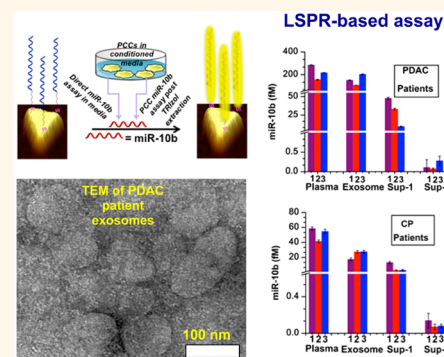
[†]Department of Chemistry and Chemical Biology, Indiana University-Purdue University Indianapolis, 402 North Blackford Street, LD 326, Indianapolis, Indiana 46202, United States

[‡]Departments of Medicine, and Biochemistry and Molecular Biology, the Indiana University Simon Cancer Center, and the Pancreatic Cancer Signature

Center, Indiana University School of Medicine, 980 West Walnut Street, R3-C528, Indianapolis, Indiana 46202, United States, and [§]Integrated Nanosystems

Development Institute, Indiana University-Purdue University Indianapolis, 402 North Blackford Street, Indianapolis, Indiana 46202, United States

ABSTRACT MicroRNAs are short noncoding RNAs consisting of 18–25 nucleotides that target specific mRNA moieties for translational repression or degradation, thereby modulating numerous biological processes. Although microRNAs have the ability to behave like oncogenes or tumor suppressors in a cell-autonomous manner, their exact roles following release into the circulation are only now being unraveled and it is important to establish sensitive assays to measure their levels in different compartments in the circulation. Here, an ultrasensitive localized surface plasmon resonance (LSPR)-based microRNA sensor with single nucleotide specificity was developed using chemically synthesized gold nanoprisms attached onto a solid substrate with unprecedented long-term stability and reversibility. The sensor was used to specifically detect microRNA-10b at the attomolar (10^{-18} M) concentration in pancreatic cancer cell lines, derived tissue culture media, human plasma, and media and plasma exosomes. In addition, for the first time, our label-free and nondestructive sensing technique was used to quantify microRNA-10b in highly purified exosomes isolated from patients with pancreatic cancer or chronic pancreatitis, and from normal controls. We show that microRNA-10b levels were significantly higher in plasma-derived exosomes from pancreatic ductal adenocarcinoma patients when compared with patients with chronic pancreatitis or normal controls. Our findings suggest that this unique technique can be used to design novel diagnostic strategies for pancreatic and other cancers based on the direct quantitative measurement of plasma and exosome microRNAs, and can be readily extended to other diseases with identifiable microRNA signatures.



KEYWORDS: gold nanoprisms · LSPR-based sensor · microRNAs · cancer biomarkers · exosomes · pancreatic cancer · chronic pancreatitis · cancer diagnosis

MicroRNAs (miRs) are small single-stranded noncoding RNAs that target specific mRNAs for translational repression or degradation and that have been implicated as key regulators in numerous biological processes.^{1–5} Altered miR expression has been reported in a variety of disease states. With respect to cancer, loss of miRs that exert tumor suppressor functions can lead to malignant

transformation and cancer progression, whereas overexpression of miRs that have oncogenic properties can promote tumor progression, invasion and metastasis.^{3,6–9} While not regulating gene expression directly, a single miR can lead to alterations in the expression of dozens or even hundreds of genes and proteins, thereby coordinately modulating a variety of cellular functions.^{1–3,8}

* Address correspondence to rsardar@iupui.edu, mkorc@iu.edu.

Received for review July 21, 2015 and accepted September 29, 2015.

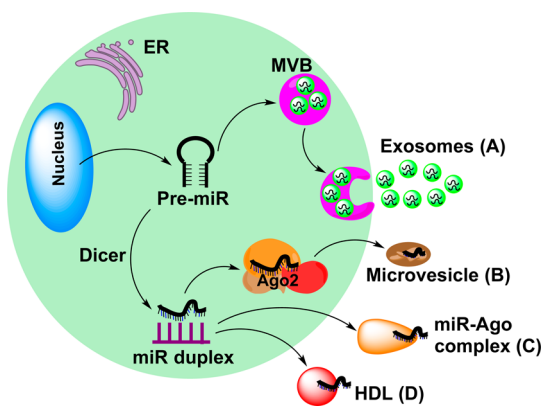
Published online October 07, 2015
10.1021/acsnano.5b04527

© 2015 American Chemical Society

Pancreatic ductal adenocarcinoma (PDAC) is a deadly cancer with an overall 5-year survival rate of 7%.¹⁰ The vast majority of PDAC patients (~80%) present with advanced disease that precludes surgical resection, yet resection is the only hope for a cure. Major causes for this late presentation of the cancer include its hidden location within the abdomen, its ability to remain symptom-free for many years prior to clinical presentation, difficulties inherent in imaging small pancreatic lesions, and the absence of PDAC-specific circulating biomarkers when the cancer is still small, symptom free, and nonmetastatic. Therefore, the identification of specific biomarkers in the circulation that will allow for the early PDAC diagnosis constitutes an urgent unmet need for this cancer.

It has been demonstrated that miR-10b is overexpressed in pancreatic cancer cells (PCCs) in PDAC,¹¹ that this overexpression is associated with shorter time to metastasis following therapy and decreased patient survival;¹² and that the plasma levels of miR-10b, miR-30c, miR-132, miR-155, and miR-212 levels can help differentiate between PDAC and individuals without pancreatic pathology.¹³ In general, miRs can be released by cancer cells through four different mechanisms. Thus, miRs can be released bound to the Ago2 protein or to high-density lipoprotein (HDL) particles, or carried as cargo within exosomes or microvesicles, as shown in Scheme 1.^{14,15} It is believed that PCCs release a preponderance of exosomes over any other type of vesicles.¹⁶ Exosomes are tiny vesicles (~40–140 nm in diameter) delineated by a lipid bilayer each of which carries a cargo of proteins, DNA, mRNAs, and miRNAs.^{17–20} They have the ability to participate in intercellular communications between cells and their microenvironments, resulting in the modulation of various cellular processes.^{17,21} It is not known, however, whether miR-10b can be released by PCCs into the medium or circulation, and whether miR-10b levels in the exosome compartment can differentiate between PDAC, chronic pancreatitis (CP), and individuals without PDAC pathology.

To quantify miR-10b release by PCCs into the circulation and to determine whether this release occurs via exosomal and/or nonexosomal compartments, it will likely be necessary to determine miR concentrations in PCC-derived conditioned media at subattomolar concentrations. In this regard, it would be extremely useful to develop highly sensitive, label-free, nondestructive, and highly specific methods for the detection and quantification of miR-10b directly in culture media, patient plasma and exosomes in both compartments. By contrast, current miR detection/quantification methods such as microarray-, real-time quantitative PCR-, electrochemical-, fluorescence-, microring resonator-, and nanopore-based techniques^{22–32} are either semi-quantitative, require amplification and labeling, or fail to work directly in biological fluids.



Scheme 1. Cellular pathways for release of microRNAs into the circulation. Exosomes are formed within multivesicular bodies (MVBs) and released into the circulation when the MVB-limiting membrane interacts with the plasma membrane.^{14,15}

Here, we report a highly specific, ultrasensitive, and regenerative localized surface plasmon resonance (LSPR)-based miR-10b sensing approach that overcomes the above limitations. The solid-state LSPR-based sensors were developed using glass substrate-bound gold nanoparticles functionalized with complementary oligonucleotides (Figure 1). Importantly, our sensor was able to distinguish between miR-10b and miR-10a, indicating that it provides for single nucleotide specificity. We also demonstrate the usefulness of miR quantification by LSPR-based technique in cultured PCCs (AsPC-1, BxPC-3, and PANC-1), derived conditioned media, and exosomes. The attomolar (aM) limit of detection (LOD), at least 1000-fold lower than current label-free methods,^{22–24,26,28,29,31,32} of our LSPR-based sensor allowed us to readily differentiate between miR-10b levels in PDAC and CP patients, and normal controls in plasma, exosomes, and post-ultracentrifugation supernatants. We propose that our label-free and ultrasensitive assay, which detects very small increases in miR-10b levels, could allow for early stage PDAC detection and permit monitoring for PDAC recurrence following therapy or resection.

RESULTS AND DISCUSSION

Fabrication of miR-10b Sensor and Characterization of Long-Term Stability and Selectivity. Solid-state, label-free biosensors have been fabricated^{33–43} using the unique LSPR-properties of metallic nanostructure.^{36–38,44} However, in most cases, the sensors failed to work in biological samples because various constituents presents in plasma and serum react with the sensors. Recently, we reported the first solid-state fabrication and characterization of miR-21 and miR-10b sensors utilizing LSPR properties of anisotropically shaped metallic nanostructures with LOD ~ 35 femtomolar (fM).⁴⁵ Our sensor could accurately quantify miR-21 in plasma from patients with PDAC. The LSPR-based sensor fabrication involved two steps: (i) covalent attachment of

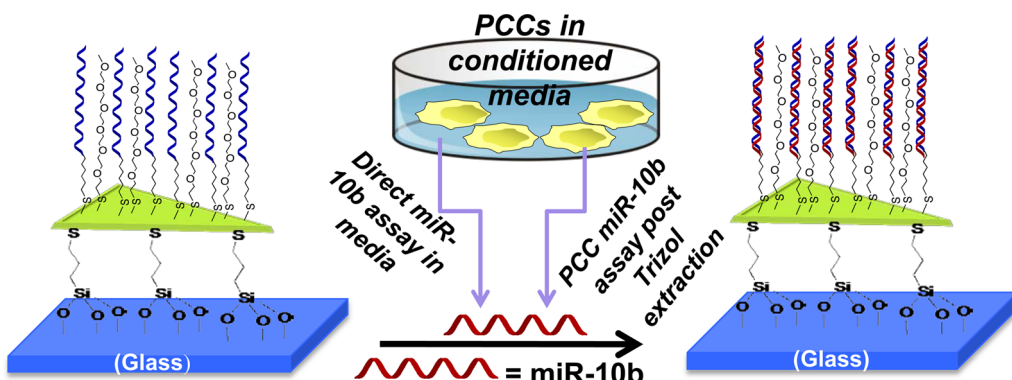


Figure 1. Schematic representation of the fabrication of the mixed -S-PEG6-SC6-ssDNA-functionalized gold nanoparticles to prepare LSPR-based sensing platform for miR-10b detection in various biological compartments. Three different edge lengths gold nanoprisms (34, 42, and 47 nm) were synthesized *via* our previously published chemical reduction method and then attached onto silanized glass surface.⁴⁵ All the surface modifications were performed in PBS buffer (pH = 7.4) under normal laboratory conditions. Detailed procedure for sensor fabrication and RNA isolation are provided in the Materials and Methods. The figure is not to scale.

chemically synthesized ~40 nm edge-length gold nanoprisms onto a silanized glass substrate; (ii) functionalization of the nanoprism surface with 1:1 mole ratio of single-stranded DNAs (HS-C6-ssDNA) and poly(ethylene glycol)6-thiols (PEG6-SH) spacer.

The LSPR-based sensing mechanism involves direct hybridization between -S-C6-ssDNA and target miRs (Figure 1) to form DNA duplex, which increases the refractive index in local dielectric environment of the nanoprisms and influences the LSPR dipole peak (λ_{LSPR}) by shifting it to higher wavelengths. LOD can be calculated from the total shift ($\Delta\lambda_{\text{LSPR}}$) versus the concentration of miRs using the empirical formula described below. The data were correlated with the widely used quantitative reverse-transcriptase-PCR (qRT-PCR) method, both techniques yielding results which were in excellent agreement. To achieve our goal of obtaining an aM LOD, we adopted the similar LSPR-based sensor fabrication technique as described previously⁴⁵ while investigating the effects of the nanoprism's edge-length on sensing efficiency and LOD. The detailed procedure for sensor fabrication is provided in the Supporting Information.

Chemically synthesized gold nanoprisms, which displayed λ_{LSPR} at 750, 800, and 820 nm in acetonitrile (Figure S1) with average edge-lengths of 34, 42, and 47 nm, respectively, as determined from scanning electron microscopy images (Figure 2A–C), were used in sensor fabrication. Figure 2E illustrates the change of λ_{LSPR} position during the functionalization of gold nanoprisms with 42 nm of average edge-length, which were attached onto silanized glass. The red-shift of the λ_{LSPR} position suggested an increase in local refractive index^{36–38,41,42,46–49} from the attachment of molecular species on the gold nanoprism's surface. The LODs of miR-10b detection for 34, 42, and 47 nm edge-length nanoprisms were calculated in human plasma and were found to be 47.5, 0.091, and 0.083 fM, respectively

(see Figure 2F and Table S2). The LODs were calculated by measuring the $\Delta\lambda_{\text{LSPR}}$ for the blank sample (mixed -S-PEG6-SC6-ssDNA-10b functionalized gold nanoprisms attached onto silanized glass substrate) and then calculating the Z (mean + 3 σ) value. The Z value was then converted into the relative concentration using the calibration curve. The data suggest that as the edge-lengths of the nanoprisms increase, their sensing volume^{40,43,50–52} also increases, thereby enhancing the LSPR sensitivity of the nanoprisms. This result is also in agreement with the literature where largest gold nanoparticles demonstrated highest LSPR-based sensing ability toward the detection of proteins.³⁵ Thus, a minute change in a nanoprism's local dielectric environment due to analyte absorption can dramatically influence the LSPR properties and λ_{LSPR} position. It is important to mention that the final λ_{LSPR} values after -ssDNA-miR-10b and miR-10b hybridization were determined in PBS buffer (wet LSPR-based sensors) instead of air in order to avoid the effects of bulk refractive index caused by the surrounding media (water). Moreover, our lowest LOD of 83 aM was more than 10⁶, 10⁴, and 10³-fold lower than the label-free fluorescent-,^{23,53} microring resonator-,^{26,29} and nanopore-based^{31,32} miR sensors, respectively. To the best of our knowledge, this is the lowest LOD reported in the literature for LSPR-based sensors for detecting any-type of biomolecules in complex physiological media such as human plasma. This label-free technique has also proven to be more sensitive than metal nanoparticle-based surface-enhanced Raman scattering sensing (LOD = 1.5 fM) of mouse pancreatic tumor.⁵⁴ At higher concentrations we observed large error bars (Figure 2F), which points to limitations of our sensing platform. However, the concentration range (10 nM to 10 pM) at which we observed this enhanced variability is well above the concentration range of the values seen in PDAC and CP patients as shown later in this article.

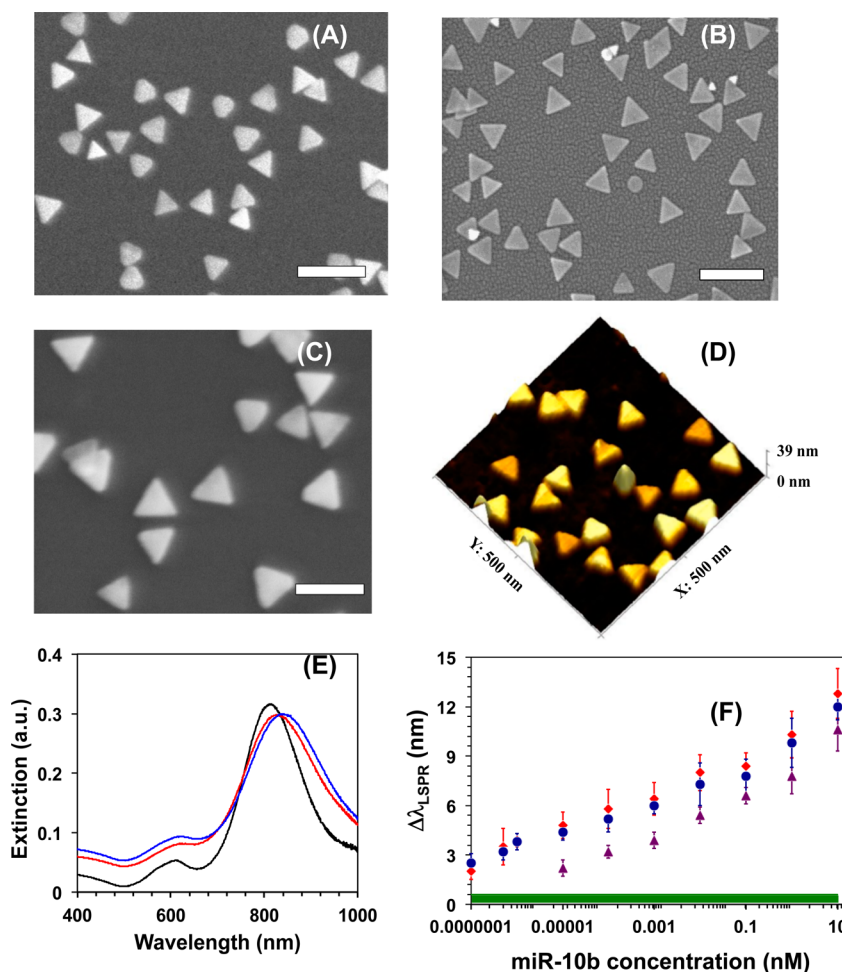


Figure 2. Scanning electron microscopy (SEM) images of three different edge-length gold nanoprisms were used for LSPR-based miR-10b sensors fabrication: (A) 34 nm, (B) 42 nm, and (C) 47 nm. Scale bars: 100 nm. (D) Atomic force microscopy image of (on the average) 42 nm edge length gold nanoprisms. (E) Changes in the LSPR dipole peak (λ_{LSPR}) position of averagely 42 nm edge length gold nanoprisms before (black) and after (red) functionalization with mixed HS-PEG6:HSC6-ssDNA-10b. The sensing platform was then rinsed with PBS buffer and incubated with 10 nM of miR-10b solution in human plasma; then, rinsed with PBS buffer and dipole peak position (blue) was determined. (F) Average λ_{LSPR} shift ($\Delta\lambda_{LSPR}$) of the sensing platforms, which were prepared with three different edge lengths nanoprisms, 34 nm (purple triangles), 42 nm (red diamonds), and 47 nm (blue dots) as a function of miR-10b concentration. All extinction spectra were measured in PBS buffer to determine the $\Delta\lambda_{LSPR}$. The green bar represents three times the standard deviation (σ) of the blank (mixed HS-PEG6:HSC6-ssDNA-10b functionalized gold nanoprisms attached onto silanized glass substrate). Inasmuch as log scale is commonly used in the LSPR biosensing literature,^{35,40,46} in order to investigate nonspecific absorption at a lower concentration range, concentrations were plotted on the axis in log scale.

The best LOD of our LSPR-based sensors were fabricated with 47 nm edge-length gold nanoprisms and demonstrated an LOD of 83.2 aM. However, functionalization of gold nanoprisms with 1:1 mole ratio of HS-C6-ssDNA-10b and PEG₆-SH shifted the λ_{LSPR} peak to ~ 863 nm. Upon further incubation with miR-10b, the λ_{LSPR} position shifted even closer to the near-infrared region, where other biological constituents present in the media and a water peak could interfere with reading the λ_{LSPR} of nanoprisms and potentially cause misleading LOD values. Therefore, we chose to use 42 nm edge length nanoprisms ($\lambda_{LSPR} = \sim 800$ nm) (LOD = 91 aM) for LSPR-based sensor fabrication for further studies as described below. The LOD was slightly lower (32.6 aM) and exhibited less background signal in the LSPR peak shift ($\Delta\lambda_{LSPR}$) in PBS buffer than

that in human plasma (91 aM) (Table S3). Our data are in agreement with the finding of a higher LSPR-based detection of streptavidin in serum by comparison with PBS buffer.⁵⁵ Therefore, it is possible that differences in ionic strength or salt concentrations between PBS buffer and plasma, in conjunction with some non-specific adsorption of plasma protein could occur on the silanized glass substrate within the sensing volume of gold nanoprisms, which could explain the slight differences in assay sensitivity between PBS buffer and human plasma.

The unprecedented sensitivity of our LSPR-based sensor fabricated with gold nanoprisms is the result of a combination of several important structural parameters. First, the atomically flat surface of the nanoprisms enables homogeneous packing between -ssDNA

and PEG spacers, which allows efficient DNA/RNA duplex formation. Second, that double-strand DNA that forms between -ssDNA/RNA displays a high charge density and the change in polarization could significantly alter the local refractive index.⁵⁶ Third, the strong electromagnetic field enhancement occurring at the sharp tips of the nanoprisms^{43,57,58} would modulate the nanoprism's LSPR properties following small changes in their local dielectric environment. Fourth, there could be a long-range charge transfer mediated by double-strand DNA, which would result in alterations in the electron density around the nanoprisms that could influence the LSPR properties. Fifth, the large sensing volume could detect minute change in the local dielectric environment due to the adsorption of analytes.

We next investigated the regeneration ability our LSPR-based sensor by hybridization and dehybridization of miR-10b for at least 5 times over a 5-day period, using the same LSPR-based sensor while monitoring the λ_{LSPR} shift, which was nearly identical each time before and after hybridization and dehybridization of miR-10b. Therefore, our sensor is highly regenerative. Furthermore, the inert character of gold nanostructures toward biological constituents present in human plasma, as well as the strong gold–sulfur bond which holds tightly the -ssDNA-10b, likely confers long-term stability to the sensors, which will enhance their potential for development into point of care diagnostic tools. We also determined that our LSPR-based sensors, which contain the specific antisense -ss-DNA-10b attached to the gold nanoprisms, are extremely specific toward their target miRs. The experimental data concerning regeneration and specificity of our sensors are provided in the Supporting Information (Figures S2 and S3) In our specificity study, 1.7 nm $\Delta\lambda_{\text{LSPR}}$ was observed when the LSPR-based sensor was incubated in a solution containing four different miRs (10 nM/miR; 40 nM total concentration). This value is very low in comparison to the 12.8 nm $\Delta\lambda_{\text{LSPR}}$ value observed upon incubation of our sensor with 10 nM miR-10b. Therefore, we believe that a $\Delta\lambda_{\text{LSPR}}$ of 1.7 nm could be due to a combination of instrumental noise and/or negligible nonspecific adsorption of miRs onto silanized glass substrate within the sensing volume of the gold nanoprisms, which was determined by us to be ~25 nm for 42 nm gold nanoprisms.⁵⁹ Importantly, at the lower concentration range (100 fM and 100 aM), the $\Delta\lambda_{\text{LSPR}}$ values were same as blank samples (data not shown).

Mir-10b has an identical seed sequence with miR-10a, but their mature forms differ at a single nucleotide. Thus, miR-10b and miR-10a contain nucleic acid A and U at the 12th position from 5' end, respectively. Moreover, the genes encoding miR-10b and 10a are located on chromosomes 2 and 17, respectively, and The Cancer Genome Atlas (TCGA) data indicate that 4% of PDACs exhibit miR-10b amplification and 4% exhibit

miR-10a amplification, but these cases are not overlapping. Therefore, we next investigated the ability of our LSPR-based sensor to distinguish between miR-10b and miR-10a using the sensor, which was constructed with mixed -SC6-ssDNA-10b-S-PEG6 in human plasma. The LSPR-based sensor displayed $\Delta\lambda_{\text{LSPR}}$ of 2.9 nm in 10 nM of miR-10a solution. This value is nearly 4.4-fold lower than $\Delta\lambda_{\text{LSPR}}$ observed for LSPR-based sensor upon incubation in 10 nM of miR-10b solution (see Figure 3A). No detectable λ_{LSPR} shift was observed when miR-10a concentration was 1.0 pM.

This result is remarkable considering there is only one nucleotide difference between miR-10b and miR-10a, and that our sensor is proposed to rely on the -ssDNA:RNA duplex formation where attachment of miR-10b/10a to nanoprism-bound -ssDNA-10b increases the local dielectric environment and modulates $\Delta\lambda_{\text{LSPR}}$. We believe that the 2.9 nm shift of $\Delta\lambda_{\text{LSPR}}$ for 10 nM of miR-10a was not controlled by the duplex formation between nanoprism-bound -ssDNA-10b and miR-10a since there is only a single nucleotide difference between them. This value is in agreement with the low molecular weight of miR-10a of ~6.9 kDa that will only influence local dielectric environment minimally, and we expect that at higher concentrations miR-10a would attach to the sensors and influence the LSPR properties.

We hypothesize that due to -ssDNA-10b and miR-10b duplex formation, a long distance charge transport takes place that alters the electron density and electromagnetic field around the nanoprisms, resulting in alteration of their LSPR properties. A long distance charge transport through a duplex DNA backbone is known to occur^{60–62} where a single base pair mismatch influences the conductivity significantly.^{60,63} Therefore, we believe in the case of duplex formation between nanoprisms bound -ssDNA-10b and miR-10a, the delocalization of free electrons of gold nanoprisms throughout the entire DNA helix did not take place, as illustrated schematically in Figure 3B,C. To test our hypothesis, we designed LSPR-based sensors by functionalizing gold nanoprisms by -SC6-ssDNA-10a-S-PEG6 and determined the sensitivity using miR-10a in human plasma where LOD was found to be an ~75 aM (data not shown). This result is expected because -ssDNA-10a and miR-10a form a duplex structure without any nucleotide mismatch, which would result free electrons delocalization.

We believe that one nucleotide difference would not alter duplex formation between -ssDNA-10b and miR-10a, and that most of the miR-10a would therefore be attached onto the sensor's surface, akin to the -ssDNA-10b/miR-10b duplex. To test our hypothesis, we quantified the level of unbound miR-10a in 1.0 nM solution after incubating with human plasma the LSPR-based sensor that was constructed with mixed -SC6-ssDNA-10b-S-PEG6. The LSPR-based sensor

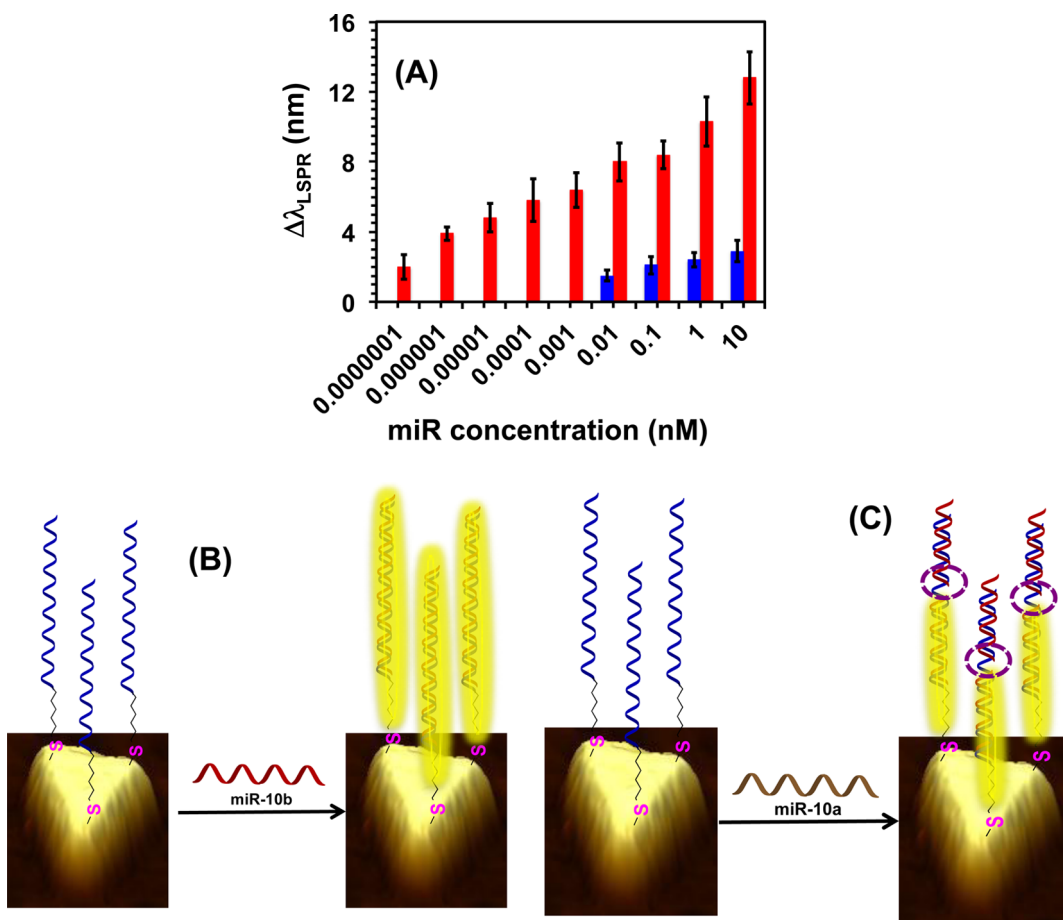


Figure 3. (A) Comparison of miR-10b (red bars) and miR-10a (blue bars) concentration-dependent LSPR responses, which were determined using LSPR-based sensors where gold nanoparticles were functionalized with -SC6-ssDNA-10b-S-PEG6. Schematic representation illustrates electron-transport through duplex DNA in LSPR-based sensor which was fabricated with -SC6-ssDNA-10b-S-PEG6 in hybridization with miR-10b (B) and miR-10a (C). The dotted circles represent broken helix structures that hinder electron transport resulting in an attenuated LSPR response.

displayed an average 2.5 nm shift of $\Delta\lambda_{LSPR}$, as expected (see Figure 3A). The miR-10a remaining in solution was then assayed using a sensor constructed with mixed -SC6-ssDNA-10a-S-PEG6, which revealed an average 6.1 nm shift in the $\Delta\lambda_{LSPR}$ (Figure S5). On the basis of our miR-10a calibration curve, this $\Delta\lambda_{LSPR}$ value corresponds to a concentration of 1.4×10^{-4} nM, which is $\sim 7 \times 10^3$ -fold lower than the original 1.0 nM miR-10a concentration. In parallel, we quantified the level of unbound miR-10b in 1.0 nM solution after incubating with human plasma the LSPR-based sensor that was constructed with mixed -SC6-ssDNA-10b-S-PEG6. A 5.4 nm shift of $\Delta\lambda_{LSPR}$ was observed, which corresponds to a concentration of 4.3×10^{-5} nM using the equation for the calibration curve reported in Table S2. This value is only 3-fold lower than the value determined for miR-10a that was free in solution after incubation into miR-10b sensors. Thus, the vast majority of miR-10a and miR-10b formed a duplex with the -ssDNA-10b-based LSPR sensor, and a single nucleotide mismatch at the 12th position did not impede miR-10a duplex formation. Our data are in agreement with reports in the literature indicating that single base

pair mismatch in duplex DNA does not alter the equilibrium constant.⁶⁴

Together, these results support our hypothesis of electron delocalization processes as a predominant factor of controlling the dramatic shift of $\Delta\lambda_{LSPR}$.

To the best of our knowledge, this is the first LSPR-based sensing approach that is able to distinguish between nucleotides having a single base pair mismatch at concentrations < 10 pM, which is at least a magnitude better than other label-free sensors.^{22,23,29,31,32} We are actively working to understand possible charge transport and/or electrons delocalization processes that could result in further improvement in the sensing ability of our LSPR-based sensors. Our experimental data are important in the context of precise quantification of miR-10b that is released by PCCs into the medium or circulation with a very low concentration as discussed below.

Quantitative Analysis of miR-10b Levels in Cultured Pancreatic Cancer Cells and their Released Products. Chemotherapy resistance occurring in conjunction with a propensity to metastasize and a lack of early stage screening procedures contributes to the high PDAC-related

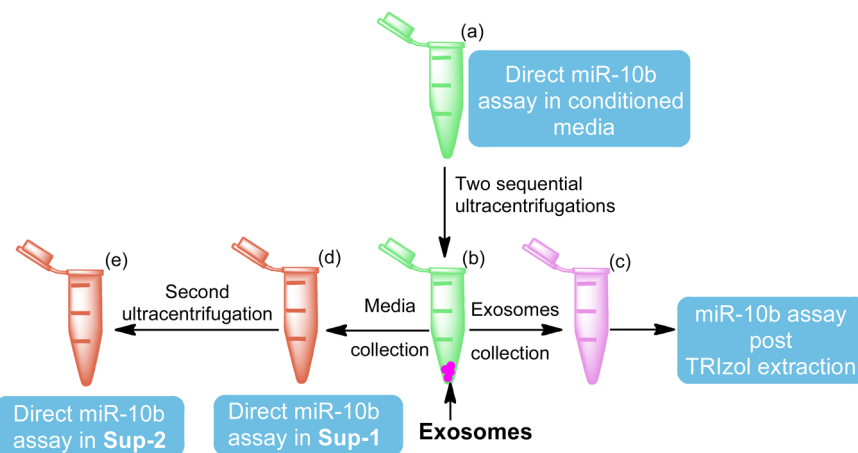


Figure 4. Schematic representation of the strategy for assaying miR-10b levels in various biological compartments by qRT-PCR and LSPR-based assay. Media from AsPC-1, BxPC-3, and PANC-1 cells, which were grown under normoxia and hypoxia conditions, were collected (a) and miR-10b was quantified by the LSPR-based technique and by qRT-PCR. Aliquots of media were subjected to two sequential ultracentrifugations (b) with an intervening PBS wash, and exosomes (c) and supernatant-1 (Sup-1, d) were collected separately. Sup-1 was again ultracentrifuged at 100 000g and Sup-2 (e) was collected. The LSPR-based technique was used to quantify miR-10b directly in Sup-1 and Sup-2, while qRT-PCR was used to determine the relative miR-10b levels after RNA extraction. No visible residue was detected after the second ultracentrifugation.

mortality. It has therefore been proposed that a non-invasive test for the early detection of PDAC could significantly improve screening strategies and ultimately lead to a vastly improved prognosis in this treatment-recalcitrant cancer.^{12,65–68} It has been suggested that miR-10b may be an ideal plasma biomarker for PDAC,^{13,69} and that glypican-1 carried by exosomes could serve as an early diagnostic marker for PDAC.⁷⁰ To further explore the possibility that circulating miR-10b could serve as a sensitive diagnostic marker for PDAC, we sought to establish a highly sensitive and quantitative assay for miR-10b concentrations in various biological compartments that include PCC-derived conditioned media, exosomes, and plasma (Figure 1). Here, for the first time we demonstrate a sensing approach which is able to precisely quantify the concentration of (i) extracted miR-10b from human PCCs, (ii) miR-10b in Roswell Park Memorial Institute (RPMI) medium and Dulbecco's modified Eagle's medium (DMEM) from these cells, (iii) extracted miR-10b from exosomes from these PCCs, and (iv) miR-10b in exosome-free supernatants (Sup) generated following two sequential ultracentrifugations (Sup-1 and Sup-2) as shown in Figure 4. Our detection method overcomes the limitation of the most widely used technique, qRT-PCR, which can only provide relative miR values rather than actual miR concentrations and which require RNA extraction procedures. Because the pancreatic tumor microenvironment (TME) is hypoxic^{71,72} and hypoxia up-regulates miR-10b expression,¹³ AsPC-1, BxPC-3, and PANC-1 cells engineered to overexpress miR-10b were grown under normoxia and hypoxia (1% O₂) conditions. By analyzing the concentration of miRs directly in media from the above PCCs as well as in exosomes released by these PCCs, We were able to investigate the proportion of miR-10b released by

PCCs directly into the culture medium by comparison to its release via exosomes.

To quantify miR-10b levels in the above PCCs, cells (4×10^5) were lysed and total RNA (including miRs) was extracted using a TRIzol kit followed by a single-step purification with the Direct-zol RNA MiniPrep kit which yielded a final elution volume of 30 μ L/sample. Next, 14 μ L from each sample was used for LSPR-based detection, whereas the remaining 14 μ L was used for qRT-PCR. We quantified miR-10b in crude media from each cell line by incubating over the LSPR-based sensor for 12 h, as described in the Materials and Methods. Subsequently, the sensors were washed with PBS buffer, and the λ_{LSPR} was measured. Figure 5A–C illustrates the LSPR-based determination of miR-10b concentrations in two types of media from three different PCCs. RPMI medium that was collected from BxPC-3 and AsPC-1 cells that were grown under hypoxia contained ~462 and 360 fM of miR-10b, respectively. DMEM collected from PANC-1 cells grown under hypoxia contained ~70 fM of miR-10b. We observed a similar pattern for miR-10b concentrations that were determined following extraction of total RNA from BxPC-3, AsPC-1, and PANC-1 cells of ~390, ~20, and ~5 fM, respectively. We also compared the LSPR-based values with qRT-PCR data from the same samples and they showed the same general trend (Figure 5D–F).

To better understand the potential pathways for miR-10b release by PCCs, we next sought to determine the concentrations of miR-10b in exosomes, and Sup-1 and Sup-2 generated following two sequential ultracentrifugations of media collected from PCCs that were cultured under hypoxia or normoxia conditions. Under hypoxia, miR-10b concentrations were ~76, ~85, and ~67 fM in exosomes collected from BxPC-3, AsPC-1, and PANC-1 cell-derived media, respectively.

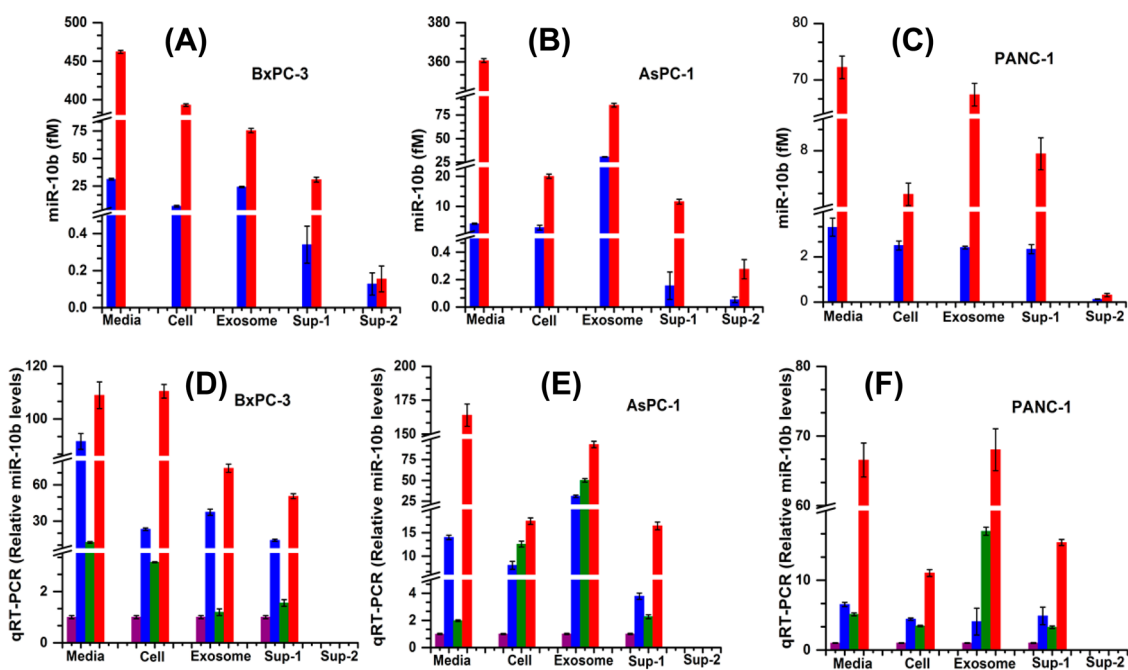


Figure 5. (A–C) Determination of miR-10b concentrations in three different pancreatic cancer cell lines under two different culture conditions, normoxia (blue bars) and hypoxia (red bars), in various biological compartments using our LSPR-based sensors. Determination of miR-10b concentrations in media, Sup-1, and Sup-2 was performed without RNA extraction, whereas total RNA was extracted from cells and exosomes. All three cell lines were engineered to overexpress miR-10b. (D–F) qRT-PCR values for normoxia (purple bars) and hypoxia (green bars) using sham-transfected pancreatic cancer cells and cells engineered to overexpress miR-10b (blue and red bars). miR-10b was assayed in total RNA extracted from media, cell, exosomes, and Sup-1 under normoxia (blue bars) and hypoxia conditions (red bars). The LSPR-based concentration and qRT-PCR fold change in miR-10b levels in cells and exosomes were determined from aliquots derived from the corresponding total RNA samples. However, by qRT-PCR, miR-10b was not detectable in Sup-2. The detailed procedure for exosomes isolation and RNAs extraction procedure are provided in the Materials and Methods.

The concentrations of miR-10b were ~31, ~12, and ~8 fM in Sup-1 from BxPC-3, AsPC-1, and PANC-1 cells, respectively, and in the ~150–300 aM range in Sup-2 (Figure 5A–C). We observed a similar trend in our qRT-PCR analysis (Figure 5D–F). This is the lowest concentration determined by any label-free miR sensors without RNA extraction.^{22–24,26,28,29,31,32,54} By contrast, we were unable to quantify miR-10b levels in sup-2 qRT-PCR. Therefore, our LSPR-based sensing technique allows for the quantitative assay of miR-10b in diverse physiological media without requiring miR extraction, and is more sensitive than the widely used qRT-PCR technique.

Using our LSPR-based technique we also determined that miR-10b levels under hypoxic conditions in exosomes were at least 3-fold (AsPC-1 and BxPC-3 cells) and as high as 28-fold (PANC-1 cells) higher than under normoxic conditions (Figure 5A–C). We also compared the LSPR-based concentration values with the qRT-PCR results (from the same sample with total RNAs extraction) and miR-10b levels exhibited the same trend by qRT-PCR as by LSPR (Figure 5D–F). To confirm that our assays measured miR-10b in exosomes, we obtained transmission electron microscopy (TEM) images of the exosomes (Figure 6), which were isolated from PANC-1 cell-derived medium. The diameters of the exosomes were easy to determine

(~60–140 nm), even though some appeared to be aggregated, which could be due to the drying process during the TEM grid preparation. The detailed procedures for exosomes collection and RNAs extraction are provided in the Materials and Methods. Our findings thus demonstrate that miR-10b concentrations are elevated under hypoxic conditions in exosomes, raising the possibility that miR-10b acts within the hypoxic TME to promote PDAC biological aggressiveness.

The data presented above on accurate quantification of miR-10b in various biological compartments using our ultrasensitive LSPR-based sensor provide insight into several important cellular processes that contribute to the release of miRs by PCCs in circulation. First, under hypoxia, miR-10b concentrations determined in exosomes collected from different cell lines were found to be comparable, and as high as 85 fM in ASPC-1 cells. Thus, PCCs release miR-10b rich exosomes into conditioned media, raising the possibility that it will be feasible to assay exosomal miRs as potential biomarkers of PDAC. Second, the concentrations of miR-10b in Sup-1 and Sup-2 were in the femtomolar and attomolar range in all three-cell lines. Therefore, some residual miRs were still present in the supernatant collected from media even after two sequential ultracentrifugations with intervening

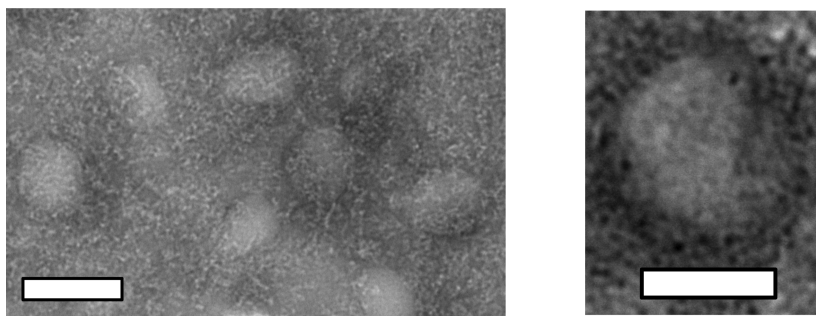


Figure 6. TEM images of exosomes collected from miR-10b overexpressing PANC-1 cells. A 10 μ L solution was drop-casted onto a formvar-coated copper grid and allowed to stand for 60 s. Excess solution was wicked away with a filter paper. A 2.0% uranyl acetate solution was applied for 10 s to negatively stain the exosomes. Scale bars: 100 nm.

washing with PBS. The presence of miR-10b in Sup-1 and Sup-2 suggests that in addition to being released *via* exosomes, miRs are released directly by PCCs into their environment. Although the specific cellular pathways for miR-10b release remain to be delineated, it is conceivable that miR-10b could detach from Ago2 protein–miR complexes as byproducts of dead cells, or be released due to the rupturing of exosomes or microvesicles because of high mechanical force applied during ultracentrifugation.^{73,74} The miR-10 concentrations in exosomes were at least 15% (BxPC-3 cells) and as high as 84% (PANC-1 cells) of total extracellular miR-10b levels (media, Sup-1 and Sup-2). Overall, we have performed the first comprehensive determination of miR concentrations at the attomolar range in various PCCs, under various growth conditions, and in different biological compartments. Our investigation has significant implications for the development of biomarkers for the early diagnosis of PDAC through isolation and quantification of circulating miR-10b, as discussed in the next section, as well as for the diagnosis of other cancers in which circulating miRs are elevated.

Exosome miR-10b Levels in Patients with Pancreatic Cancer and Chronic Pancreatitis. Although hundreds of human miRs are known, their exact role in various aspects of cancer progression and modulation of cell proliferation, apoptosis, and metastasis is yet to be delineated. Importantly, these small, noncoding RNAs have the potential to serve as diagnostic markers for different diseases including PDAC. Plasma miR-10b levels, as determined by qRT-PCR, are elevated in PDAC patients by comparison with CP patients and normal control subjects or patients with gall-bladder disease.^{13,69} However, PCR-based assays require RNA extraction and purification, are only semiquantitative, and are not sufficiently sensitive to differentiate miR-10b levels in patients with CP from levels in normal controls.¹³ As demonstrated above, our label-free, LSPR-based detection technique is able to assay attomolar concentrations of miR-10b directly not only in conditioned media, but also in PCC-derived exosomes. Therefore, it would be a breakthrough to establish an analytical

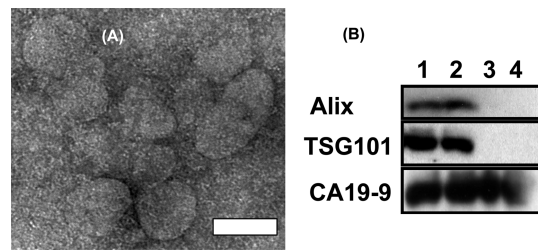


Figure 7. (A) A representative TEM image showing exosomes of \sim 50–120 nm in diameter. Plasma from a patient with PDAC (500 μ L) was ultracentrifuged twice, the pellets were suspended in 100 μ L of 2% glutaraldehyde/2% paraformaldehyde solution, and a 10 μ L aliquot was drop-casted onto a formvar-coated copper grid. The solution was allowed to stand for 60 s, and excess solution was wicked away with a filter paper. A 2.0% uranyl acetate solution was applied for 10 s to negatively stain the exosomes. Scale bar: 100 nm. (B) Immunoblotting of plasma-derived exosomes and plasma validates ultracentrifugation method. Plasma samples from two PDAC patients (500 μ L/sample) were cleared of cellular debris by centrifugation at 10 000g (4 °C) for 30 min. Supernatants were transferred to a new tube and subjected to ultracentrifugation at 100 000g for 70 min (4 °C). The exosome pellets (lanes 1 and 2) were washed with PBS and subjected to a second ultracentrifugation. Pellets were then suspended in 40 μ L of protein lysis buffer as previously described.⁶⁹ The corresponding exosome-depleted plasma (50 μ L/sample) aliquots (lanes 3 and 4) were also subjected to immunoblotting following addition of an equal volume of 2 \times lysis buffer. Samples (20 μ L each; 1 μ g/ μ L) were loaded on a 10% acrylamide gel and immunoblotting was performed using anti-Alix, anti-Tsg101, and anti-CA19-9 antibodies.⁶⁹

technique that could be used to detect and quantify miR-10b directly in crude plasma samples.

Here, we report as a proof of principle, the first label-free assay to quantify and compare the miR levels between patients with PDAC ($n = 3$), CP ($n = 3$), and normal controls ($n = 3$). Moreover, we determined the concentration of miR-10b in crude plasma, exosomes, and Sup-1 and Sup-2. The exosomes were collected from plasma through ultracentrifugation as described in the Materials and Methods. Figure 7A illustrates the TEM image of exosomes collected from plasma of a PDAC patient. A brief TRIZol extraction, followed by a single-step purification using the direct-zol RNA MiniPrep kit makes our assay simple and innovative.

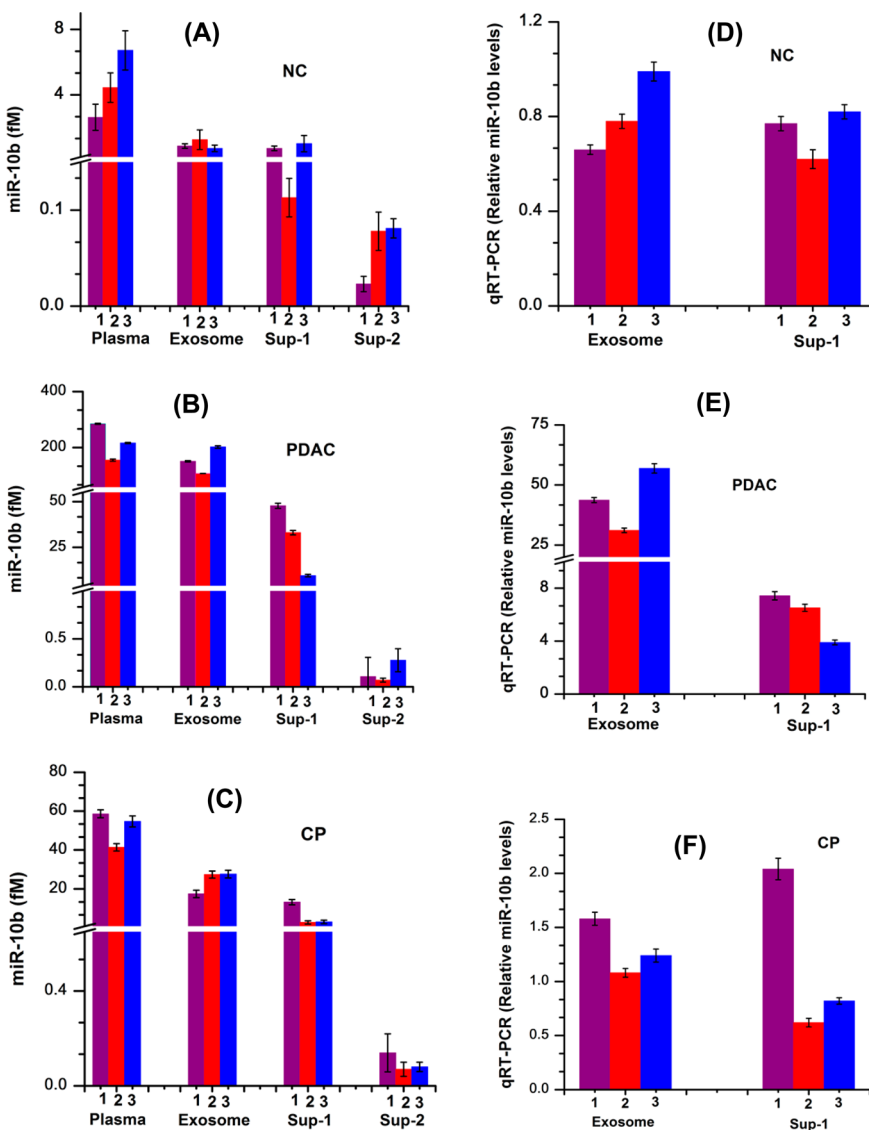


Figure 8. (A–C) Determination of miR-10b concentration in plasma samples from three normal control (NC), three patients with PDAC, and three patients with CP using our LSPR-based sensors. Determination of miR-10b levels in plasma, Sup-1, and Sup-2 was performed without RNA extraction, whereas total RNA was extracted from exosomes. (D–F) qRT-PCR values for miR-10b from total RNA extracted from exosomes and Sup-1 in three NC, three patients with PDAC, and three patients with CP. The LSPR-based concentration and qRT-PCR values for miR-10b in exosomes were determined from the same RNA samples from each subject, all performed in a blinded manner. Each color represents a different PDAC, CP, or control subject. MiR-10b levels in Sup-2 were below the level of detection by qRT-PCR and, hence, are not shown.

Exosomes are of endosomal origin and therefore express endosomal proteins such as tumor susceptibility gene 101 (Tsg101) and Alix.¹⁵ Exosomes that are of PDAC origin are also expected to express carbohydrate-associated 19-9 (CA19-9), which is a well-known pancreatic tumor marker in the circulation.⁷⁵ To confirm that our plasma ultracentrifugation procedures yielded PDAC-derived exosomes, lysates of freshly isolated exosomes (20 µg/sample) and 50 µL of plasma supernatants were subjected to immunoblotting for TSG1, Alix, and CA19-9 (Figure 7B). Our data show that plasma exosomes from PDAC patients express Alix, Tsg101, and CA19-9, and that neither Alix nor Tsg101 is present in the plasma following the initial

ultracentrifugation (Figure 7B). By contrast, CA19-9, as expected, is present in exosome-depleted plasma.

The concentrations of miR-10b in different biological compartments were determined using our LSPR-based assay, as shown in Figure 8A–C. All three samples from PDAC patients exhibited high levels of miR-10b in both plasma and circulating exosomes (Figure 8B). By contrast, the same LSPR-based assay revealed that miR-10b levels in plasma and exosomes from normal controls (Figure 8A) and CP patients (Figure 8C) were 50- to 60-fold lower and 4- to 10-fold lower, respectively, than those in the corresponding PDAC samples. Importantly, miR-10b levels in the CP samples (Figure 8C) were significantly higher than

those in normal controls (Figure 8A). Figure 8D–F shows the relative miR-10b levels determined by qRT-PCR. Supporting Information Table S7 provides the *p*-values for the statistical analysis that was performed to compare PDAC, CP, and normal controls. Thus, our LSPR-based assay indicates that there are very high levels of miR-10b in the exosomes isolated from the plasma of PDAC patients (Figure 8), which is in contrast to observations in plasma from breast cancer patients where only 5% of miR-16, miR-21, and miR-24 were in the exosome compartment.⁷³ Taken together, our data validate our hypothesis that PCCs are prone to release miR-10b as cargo within exosomes.

Comparing our LSPR- and qRT-PCR-based data, we can draw several conclusions regarding our unique label-free technique. First, the trend of LSPR-based miR-10b concentration in exosomes and Sup-1 of three PDAC, three CP, and three normal control samples is identical to the well-established and most widely used, qRT-PCR technique, underscoring the reliability of our nanoprisms-based detection technique. Second, miR-10b levels in PDAC and CP samples were quantified directly in patient plasma, which cannot be accomplished by qRT-PCR. Third, the LSPR-based assay was able to quantify miR-10b level in Sup-2, but we were unable to extract sufficient RNAs from Sup-2 for quantification by qRT-PCR. This is because the LSPR-based technique did not require any RNA extraction method, and is able to detect miR-10b in the subattomolar concentration range. Fourth, while qRT-PCR fails to differentiate between miR-10b levels in patients with CP by comparison with normal controls (see Figure 8), the ultrasensitive LSPR-based sensor shows that plasma miR-10b levels are significantly higher in CP patients when compared to levels in normal controls. Moreover, there was at least a 5-fold increase in miR-10b levels in either plasma or exosomes in patients with CP when compared with normal controls. Thus, our LSPR-based detection technique displays unique aspects of modern analytical methodology that allows us to precisely quantify miRs at very low concentrations which is not feasible with any other known techniques.

CP is a chronic inflammatory condition of the pancreas associated with variable degrees of fibrosis which can lead to significant pancreatic exocrine and endocrine dysfunction, glucose intolerance, and diabetes.⁷⁶ Although most patients with CP do not develop PDAC, it is well established that CP is associated with a higher risk for developing PDAC.⁷⁷ However, there are no markers that will help stratify CP patients with respect to their risk for developing PDAC. Our observations that CP patients exhibit slight but significant increases in miR-10b levels in both the plasma and circulating exosomes by comparison with normal controls raise the possibility that monitoring for rising miR-10b levels in CP patients by using our ultrasensitive LSPR-based sensor could identify those

patients that are at a high risk for developing PDAC and that need further evaluation by procedures such as endoscopic ultrasonography, thereby allowing for the early detection of CP progression to PDAC.

Our LSPR-based quantification showed that miR-10b is present at high concentrations (\sim 210 fM) in exosomes isolated from the plasma of PDAC patients, whereas the supernatants post-centrifugation (Sup-1, \sim 10–50 fM; and Sup-2, 70–300 aM) had exceedingly low miR-10b levels. Therefore, the vast majority of miR-10b that is released by PCCs is present in the exosomes. Importantly, analysis of the TCGA data for PDAC revealed that many of the PDAC tissue samples in TCGA exhibit increased miR-10b expression, ranging as high as \sim 180 000 reads per million (RPM). Moreover, there are five Stage IA and eight stage IB PDAC cases in the TCGA data, with mean miR-10b values of 13 400 and 15 225 RPM, respectively, indicating that miR-10b is already elevated at the earliest stages of clinical presentation for PDAC. Our simple, label-free, highly specific, and regenerative LSPR-based sensors would thus allow for quantitative measurements of miR-10b circulating in exosomes, which could serve as a biomarker for early PDAC diagnosis. Importantly, the working principle of our LSPR-based sensor is that the attachment of miR-10b to nanoprisms-bound ssDNA-10b increases the local dielectric environment and modulates $\Delta\lambda_{\text{LSPR}}$. Therefore, modifying the surface of the nanoprisms by any type of ssDNA would allow for the quantitative detection of any complementary miR-X (for example, X = 30c, 106b, 155, and 212) that is overexpressed in PDAC.¹³ We believe that our ultrasensitive assay will allow for the detection in plasma of miRs that are under-expressed in PDAC and other pathological conditions, and we have initiated the development of additional LSPR-based sensors that could quantify miR-X level, including those with single nucleotide specificity, in biological fluids and exosomes.

CONCLUSION

In conclusion, we have demonstrated a simple and novel ultrasensitive LSPR-based sensing platform that enables a quantitative determination of miR-10b in biological fluids and exosomes with a single nucleotide specificity at the attomolar concentration. We believe that the high sensitivity of our LSPR-based sensor is due to charge transport and/or delocalization of free electrons of the gold nanoprisms through DNA backbone when ssDNA forms the duplex and becomes double-stranded. Our label-free LSPR-based detection technique provides a unique opportunity for bypassing current detection approaches that require complicated fabrication methods or extra-labeling, and that fail to work in complex biological fluids. Moreover, our LSPR-based sensor is regenerative through multiple cycles and stable for at least 5 days without diminution in sensitivity. The LSPR-based assay has also

demonstrated that miR-10b release *via* exosomes by PCCs is greatly enhanced under hypoxic conditions. We have also shown the versatility of our detection technique through precise quantification of miR-10b without any RNA extraction method in plasma of patients with PDAC and CP, and reliably differentiate between patients with CP and normal controls. To the best of our knowledge, this is the first demonstration of a label-free technique to quantify miRs in exosomes

and the first report to show that miR-10b is abundant in circulating exosomes in PDAC patients. Future studies are required to validate the diagnostic accuracy of this technique in larger cohorts. We believe that our novel sensing platform, which enables quantification of attomolar concentrations of miR biomarkers from biological fluids without requiring extensive sample preparation, may also have prognostic and therapeutic implications.

MATERIALS AND METHODS

Materials. Chloro(triethylphosphine) gold(I) (Et_3PAuCl , 97%), poly(methylhydrosiloxane) (PMHS, Mn = 1700–3300), trioctylamine (TOA, 98%), ACS grade acetonitrile (CH_3CN , 99.9%), methanol (99.8%), human plasma (contains 4% trisodium citrate and tested for HIV, hepatitis C and hepatitis B), thiol modified ssDNAs, microRNAs (miRs), Tris-base, magnesium chloride (MgCl_2), and potassium chloride (KCl) were purchased from Sigma-Aldrich and were used as received. (3-Mercaptopropyl)-triethoxysilane (MPTES, 94%) was purchased from Alfa Aesar, and ethanol (alcohol 200 proof) was purchased from Decon labs. RNase H enzyme and RNase H reaction buffer were purchased from New England Bio Labs, Inc. RNase-free sterile water was obtained from Baxter Healthcare Corporation. 1, 4-Dithiothreitol (DTT) was purchased from Roche Diagnostics. Anti-Alix (1:1000 dilution) was from Sigma, anti-Tsg101 (1:200 dilution) from Santa Cruz, and anti-CA19-9 (1:200 dilution) from Abcam. Hydrochloric acid (HCl), sodium chloride (NaCl, ≥99.5%), sodium phosphate monobasic monohydrate ($\text{NaH}_2\text{PO}_4 \cdot \text{H}_2\text{O}$, >98%), sodium phosphate dibasic anhydrous (Na_2HPO_4), and the glass coverslips were purchased from Fisher Scientific. RBS 35 Detergent was obtained from Thermo Scientific and used as received. The super Sharpe silicon scanning probes (SSS-NCHR) for atomic force microscopy measurements were purchased from nanosensors. All water was purified using a Thermo Scientific Barnstead Nanopure system. Thiol modified oligonucleotides and all miRs were stored at –20 °C. RNase-free sterile water was used to prepare the PBS buffer solution. Polyethylene glycol thiol (PEG6-SH) was synthesized in our laboratory using published procedures.⁷⁸ TRIzol and TRIzol LS were purchased from Life Technologies. Direct-zol RNA MiniPrep kit was purchased from Zymo Research.

Synthesis of Gold Nanoprisms with Various Edge Lengths. Gold nanoparticles were chemically synthesized according to our previously developed procedure with minor modification.^{59,79} Specifically, $\text{Et}_3\text{PAu}(\text{I})\text{Cl}$ (8 mg, 0.02 mmol) was dissolved in 5 mL of acetonitrile and allowed to stir for 5 min at room temperature in an Erlenmeyer flask. A total of 0.085 mL of TOA and 0.3 mL of PMHS were mixed with 1 mL of acetonitrile in a vial and injected into the above solution. The reaction mixture was then allowed to heat at 40 °C. The solution color started to change from colorless to pink, purple, blue, and at this point, 14 mL of acetonitrile was added to the reaction and the reaction was allowed to run for another 60 min, which resulted in a dark blue solution indicating the formation of nanoparticles with a stable localized surface plasmon resonance dipole peak (λ_{LSPR}) at 750 nm in acetonitrile (Figure S1 and Table S2). At this point, the solution was removed from heat, centrifuged at 7000 rpm for 2 min, and used to fabricate LSPR-based sensors. The SEM analysis confirmed an average edge-length of 34 nm. Gold nanoparticles with an average 42 nm ($\lambda_{\text{LSPR}} = 800$ nm) and 47 nm ($\lambda_{\text{LSPR}} = 820$ nm) edge-length were synthesized using identical mole ratio of Et_3PAuCl and PMHS, but changing the TOA amount of 0.095 and 0.1 mL, respectively.

Fabrication of LSPR-Based miR-10b Sensors. The gold nanoparticles containing LSPR-based sensors for miR-10b detection were developed using our published method.⁴⁵ A tape cleaning procedure was carried out, in order to remove the nonprismatic nanostructures from the coverslips. Adhesive tape was applied to the gold nanoparticles-bound substrate surface, gently pressed

down with a finger, and then slowly removed at a 90° angle. The nanoprisms-bound substrates were subjected to overnight incubation in a solution of PBS that contained a 1:1 ratio of 1.0 μM solution of HS-C6-ssDNA-10b and HS-PEG6. Finally, the -S-C6-ssDNA-10b and -S-PEG6 functionalized nanoprisms were rinsed with adequate amount of PBS buffer solution to remove non-specifically bound thiols. These functionalized nanoprisms, which were covalently attached onto supporting substrate and denoted as the LSPR-based sensor, were further utilized for miR-10b detection. We obtained the concentration of miR-10b in each media from the observed λ_{LSPR} shift and converted it into the corresponding concentration using the calibration curve derived for miR-10b under various conditions, which include two different physiological media (human plasma and PBS buffer), two different culture media (RPMI and DMEM) and two different growth conditions (normoxia and hypoxia) (see Supporting Information Figure S4 and Table S3).

Cell Culture. Stably overexpressing miR-10b and control ASPC-1, BxPC-3, and PANC-1 cells from ATCC (Manassas, VA) were grown in culture at 37 °C, 5% CO₂ in either RPMI 1640 (ASPC-1 and BxPC-3) or DMEM (PANC-1) with 5% FBS (exosomes depleted) and 1% penicillin/streptomycin as described previously by our group.⁶⁹ Cells were plated in 60 mm dishes at a concentration of 4×10^5 and grown in standard conditions (normoxia) for 72 h. For hypoxic conditions, plates were removed from normoxia at 24 h post-plating and transferred to a hypoxia chamber at 37 °C, 5% CO₂, and 1% O₂ for 48 h.

Engineered miR-10b PCCs and RNA Isolation. Cells were stably transduced to overexpress miR-10b with the MDH1-PGK-GFP microRNA-10b retroviral construct (Addgene plasmid 16070) with packaging plasmids PAX2 and pMD2.G. Sham-transfections to generate control cells were established by transduction with an empty MDH1-PGK-GFP construct (Addgene plasmid 11375) using Phoenix cells for retroviral packaging (Life Technologies). Harvested viruses were used for transduction as previously described,⁸⁰ and GFP-positive cells were isolated using flow cytometry 48 h post-transduction (Flow Cytometry Facility, Indiana University School of Medicine, Indianapolis, IN, USA). Sorted cells were plated and cultured as described above and allowed to recover for 48 h prior to use in experiments. Validation of continued miR-10b overexpression was confirmed by monitoring GFP fluorescence and miR-10b levels by qRT-PCR. RNA was isolated from cells using TRIzol, or from media using TRIzol LS according to manufacturer's protocol.

Exosome Isolation from Plasma and RNA Isolation. Plasma samples from PDAC, CP, and normal controls (500 μL /sample) were centrifuged at 10 000g (4 °C) for 30 min. Supernatants were transferred to a new tube and subjected to ultracentrifugation at 100 000g for 70 min (4 °C). The supernatant was removed to a new tube for analysis, the pellet was washed with 1× PBS, and ultracentrifugation was repeated. RNA isolation (100 μL /plasma sample) was performed using the TRIzol kit followed by a single-step purification with the Direct-zol RNA MiniPrep kit (Zymo Research).

LSPR-Based Quantification of Plasma and Exosomal miR-10b. Plasma (100 μL) from either PDAC or CP patients was diluted with 2.5 mL of PBS buffer. The LSPR-based sensors were incubated overnight and then rinsed with PBS buffer, and extinction spectra were collected in PBS buffer to quantify the miR-10b levels.

For exosomal miR-10b quantification, 20 μ L of the TRizol isolate was subjected to a single-step purification procedure with Direct-zol, and the sample was diluted with 2.0 mL of PBS buffer and incubated overnight with LSPR-based sensors. In this case, the extinction spectra were collected in PBS buffer. For accurate quantification of miR-10b in each compartment, each PDAC, CP, and normal control sample was assayed twice using a total of 10 sensors.

Conflict of Interest: The authors declare no competing financial interest.

Acknowledgment. This work was supported in part by IUPUI FORCES funding (R.S. and M.K.), an Indiana University IUCRG grant (R.S. and M.K.), an award from the Integrated Nanosystems Development Institute (R.S.), and U.S. Public Health Service Grant CA-75059, awarded by the National Cancer Institute to M.K. S.M. thanks ACS Project SEED program for financial support. We thank the Indiana University Simon Cancer Center Tissue Bank for human plasma samples, and the Indiana University Electron Microscopy center for assistance with transmission electron microscopy imaging. We also thank A. Siegel and S. Savant for valuable advice regarding the manuscript. R.S. and M.K. supervised research. G.K.J. designed LSPR experiments and G.K.J., T.L., and S.M. collected all the optical data. S.D.-M. conducted cell culture studies, established miR-10b overexpressing cells, carried out statistical analysis, RNA extraction from various biological compartments including PDAC and CP patient samples and normal control samples, and qRT-PCR analysis. G.K.J. and R.S. performed SEM and TEM analyses, respectively. K.L. performed the PEG synthesis. G.K.J., R.S., and M.K. wrote the manuscript.

Supporting Information Available: The Supporting Information is available free of charge on the ACS Publications website at DOI: 10.1021/acsnano.5b04527.

Additional experimental details, tables, UV-vis extinction spectra, calibration curves, and statistical data (PDF)

REFERENCES AND NOTES

- Bartel, D. P. MicroRNAs: Genomics, Biogenesis, Mechanism, and Function. *MicroRNAs: Genomics, Biogenesis, Mechanism, and Function*. *Cell* **2004**, *116*, 281–297.
- Winter, J.; Jung, S.; Keller, S.; Gregory, R. I.; Diederichs, S. Many roads to maturity: microRNA biogenesis pathways and their regulation. Many roads to maturity: microRNA biogenesis pathways and their regulation. *Nat. Cell Biol.* **2009**, *11*, 228–234.
- Esquela-Kerscher, A.; Slack, F. J. Oncomirs - microRNAs with a role in cancer. Oncomirs - microRNAs with a role in cancer. *Nat. Rev. Cancer* **2006**, *6*, 259–269.
- He, L.; Thomson, J. M.; Hemann, M. T.; Hernando-Monge, E.; Mu, D.; Goodson, S.; Powers, S.; Cordon-Cardo, C.; Lowe, S. W.; Hannon, G. J.; et al. A microRNA polycistron as a potential human oncogene. A microRNA polycistron as a potential human oncogene. *Nature* **2005**, *435*, 828–833.
- Lu, J.; Getz, G.; Miska, E. A.; Alvarez-Saavedra, E.; Lamb, J.; Peck, D.; Sweet-Cordero, A.; Ebert, B. L.; Mak, R. H.; Ferrando, A. A.; et al. MicroRNA expression profiles classify human cancers. MicroRNA expression profiles classify human cancers. *Nature* **2005**, *435*, 834–838.
- Devulapally, R.; Sekar, N. M.; Sekar, T. V.; Foygel, K.; Massoud, T. F.; Willmann, J. K.; Paulmurugan, R. Polymer Nanoparticles Mediated Codelivery of AntimiR-10b and AntimiR-21 for Achieving Triple Negative Breast Cancer Therapy. Polymer Nanoparticles Mediated Codelivery of AntimiR-10b and AntimiR-21 for Achieving Triple Negative Breast Cancer Therapy. *ACS Nano* **2015**, *9*, 2290–2302.
- Chiang, A. C.; Massagué, J. Molecular Basis of Metastasis. Molecular Basis of Metastasis. *N. Engl. J. Med.* **2008**, *359*, 2814–2823.
- Lin, S.; Gregory, R. I. MicroRNA biogenesis pathways in cancer. MicroRNA biogenesis pathways in cancer. *Nat. Rev. Cancer* **2015**, *15*, 321–333.
- Ma, L.; Teruya-Feldstein, J.; Weinberg, R. A. Tumour invasion and metastasis initiated by microRNA-10b in breast cancer. *Nature* **2007**, *449*, 682–688.
- Siegel, R.; Ma, J.; Zou, Z.; Jemal, A. Cancer statistics, 2014. Cancer statistics, 2014. *Ca-Cancer J. Clin.* **2014**, *64*, 9–29.
- Sempere, L. F.; Preis, M.; Yezefski, T.; Ouyang, H.; Suriawinata, A. A.; Silahtaroglu, A.; Conejo-Garcia, J. R.; Kauppinen, S.; Wells, W.; Korc, M. Fluorescence-Based Codetection with Protein Markers Reveals Distinct Cellular Compartments for Altered MicroRNA Expression in Solid Tumors. *Clin. Cancer Res.* **2010**, *16*, 4246–4255.
- Preis, M.; Gardner, T. B.; Gordon, S. R.; Pipas, J. M.; Mackenzie, T. A.; Klein, E. E.; Longnecker, D. S.; Gutmann, E. J.; Sempere, L. F.; Korc, M. MicroRNA-10b Expression Correlates with Response to Neoadjuvant Therapy and Survival in Pancreatic Ductal Adenocarcinoma. *Clin. Cancer Res.* **2011**, *17*, 5812–5821.
- Cote, G. A.; Gore, A. J.; McElvea, S. D.; Heathers, L. E.; Xu, H.; Sherman, S.; Korc, M. A Pilot Study to Develop a Diagnostic Test for Pancreatic Ductal Adenocarcinoma Based on Differential Expression of Select miRNA in Plasma and Bile. *Am. J. Gastroenterol.* **2014**, *109*, 1942–1952.
- D'Souza-Schorey, C.; Clancy, J. W. Tumor-derived microvesicles: shedding light on novel microenvironment modulators and prospective cancer biomarkers. *Genes Dev.* **2012**, *26*, 1287–1299.
- Raposo, G.; Stoorvogel, W. Extracellular vesicles: Exosomes, microvesicles, and friends. *J. Cell Biol.* **2013**, *200*, 373–383.
- Javeed, N.; Sagar, G.; Dutta, S. K.; Smyrk, T. C.; Lau, J. S.; Bhattacharya, S.; Truty, M.; Petersen, G. M.; Kaufman, R. J.; Chari, S. T.; et al. Pancreatic Cancer—Derived Exosomes Cause Paraneoplastic β -cell Dysfunction. *Clin. Cancer Res.* **2015**, *21*, 1722–1733.
- Thakur, B. K.; Zhang, H.; Becker, A.; Matei, I.; Huang, Y.; Costa-Silva, B.; Zheng, Y.; Hoshino, A.; Brazier, H.; Xiang, J.; et al. Double-stranded DNA in exosomes: a novel biomarker in cancer detection. *Cell Res.* **2014**, *24*, 766–769.
- Tetta, C.; Ghigo, E.; Silengo, L.; Dereghibus, M.; Camussi, G. Extracellular vesicles as an emerging mechanism of cell-to-cell communication. *Endocrine* **2013**, *44*, 11–19.
- Valadi, H.; Ekstrom, K.; Bossios, A.; Sjostrand, M.; Lee, J. J.; Lotvall, J. O. Exosome-mediated transfer of mRNAs and microRNAs is a novel mechanism of genetic exchange between cells. *Nat. Cell Biol.* **2007**, *9*, 654–659.
- Choi, D.-S.; Kim, D.-K.; Kim, Y.-K.; Gho, Y. S. Proteomics, transcriptomics and lipidomics of exosomes and ectosomes. *Proteomics* **2013**, *13*, 1554–1571.
- Costa-Silva, B.; Aiello, N. M.; Ocean, A. J.; Singh, S.; Zhang, H.; Thakur, B. K.; Becker, A.; Hoshino, A.; Mark, M. T.; Molina, H.; et al. Pancreatic cancer exosomes initiate pre-metastatic niche formation in the liver. *Nat. Cell Biol.* **2015**, *17*, 816.
- Dorvel, B. R.; Reddy, B.; Go, J.; Duarte Guevara, C.; Salm, E.; Alam, M. A.; Bashir, R. Silicon Nanowires with High-k Hafnium Oxide Dielectrics for Sensitive Detection of Small Nucleic Acid Oligomers. *ACS Nano* **2012**, *6*, 6150–6164.
- Ryoo, S.-R.; Lee, J.; Yeo, J.; Na, H.-K.; Kim, Y.-K.; Jang, H.; Lee, J. H.; Han, S. W.; Lee, Y.; Kim, V. N.; et al. Quantitative and Multiplexed MicroRNA Sensing in Living Cells Based on Peptide Nucleic Acid and Nano Graphene Oxide (PANGO). *ACS Nano* **2013**, *7*, 5882–5891.
- Gao, Z.; Deng, H.; Shen, W.; Ren, Y. A Label-Free Biosensor for Electrochemical Detection of Femtomolar MicroRNAs. *Anal. Chem.* **2013**, *85*, 1624–1630.
- Li, J.; Yao, B.; Huang, H.; Wang, Z.; Sun, C.; Fan, Y.; Chang, Q.; Li, S.; Wang, X.; Xi, J. Real-Time Polymerase Chain Reaction MicroRNA Detection Based on Enzymatic Stem-Loop Probes Ligation. *Anal. Chem.* **2009**, *81*, 5446–5451.
- Qavi, A. J.; Kindt, J. T.; Gleeson, M. A.; Bailey, R. C. Anti-DNA: RNA Antibodies and Silicon Photonic Microring Resonators: Increased Sensitivity for Multiplexed microRNA Detection. *Anal. Chem.* **2011**, *83*, 5949–5956.
- Zhou, W.-J.; Chen, Y.; Corn, R. M. Ultrasensitive Microarray Detection of Short RNA Sequences with Enzymatically Modified Nanoparticles and Surface Plasmon Resonance Imaging Measurements. *Anal. Chem.* **2011**, *83*, 3897–3902.

28. Lee, J. M.; Cho, H.; Jung, Y. Fabrication of a Structure-Specific RNA Binder for Array Detection of Label-Free MicroRNA. *Angew. Chem., Int. Ed.* **2010**, *49*, 8662–8665.
29. Qavi, A. J.; Bailey, R. C. Multiplexed Detection and Label-Free Quantitation of MicroRNAs Using Arrays of Silicon Photonic Microring Resonators. *Angew. Chem., Int. Ed.* **2010**, *49*, 4608–4611.
30. Fang, S.; Lee, H. J.; Wark, A. W.; Corn, R. M. Attomole Microarray Detection of MicroRNAs by Nanoparticle-Amplified SPR Imaging Measurements of Surface Polyadenylation Reactions. *J. Am. Chem. Soc.* **2006**, *128*, 14044–14046.
31. Wang, Y.; Zheng, D.; Tan, Q.; Wang, M. X.; Gu, L.-Q. Nanopore-based detection of circulating microRNAs in lung cancer patients. *Nat. Nanotechnol.* **2011**, *6*, 668–674.
32. Wanunu, M.; Dadosh, T.; Ray, V.; Jin, J.; McReynolds, L.; Drndic, M. Rapid electronic detection of probe-specific microRNAs using thin nanopore sensors. *Nat. Nanotechnol.* **2010**, *5*, 807–814.
33. Dondapati, S. K.; Sau, T. K.; Hrelescu, C.; Klar, T. A.; Stefani, F. D.; Feldmann, J. Label-free Biosensing Based on Single Gold Nanostars as Plasmonic Transducers. *ACS Nano* **2010**, *4*, 6318–6322.
34. Otte, M. A.; Sepulveda, B.; Ni, W.; Juste, J. P.; Liz-Marzan, L. M.; Lechuga, L. M. Identification of the Optimal Spectral Region for Plasmonic and Nanoplasmatic Sensing. *ACS Nano* **2010**, *4*, 349–357.
35. Nath, N.; Chilkoti, A. Label-Free Biosensing by Surface Plasmon Resonance of Nanoparticles on Glass: Optimization of Nanoparticle Size. *Anal. Chem.* **2004**, *76*, 5370–5378.
36. Willets, K. A.; Van Duyne, R. P. Localized Surface Plasmon Resonance Spectroscopy and Sensing. *Annu. Rev. Phys. Chem.* **2007**, *58*, 267–297.
37. Halas, N. J.; Lal, S.; Chang, W.-S.; Link, S.; Nordlander, P. Plasmons in Strongly Coupled Metallic Nanostructures. *Chem. Rev.* **2011**, *111*, 3913–3961.
38. Mayer, K. M.; Hafner, J. H. Localized Surface Plasmon Resonance Sensors. *Chem. Rev.* **2011**, *111*, 3828–3857.
39. Stewart, M. E.; Anderton, C. R.; Thompson, L. B.; Maria, J.; Gray, S. K.; Rogers, J. A.; Nuzzo, R. G. Nanostructured Plasmonic Sensors. *Chem. Rev.* **2008**, *108*, 494–521.
40. Haes, A. J.; Van Duyne, R. P. A Nanoscale Optical Biosensor: Sensitivity and Selectivity of an Approach Based on the Localized Surface Plasmon Resonance Spectroscopy of Triangular Silver Nanoparticles. *J. Am. Chem. Soc.* **2002**, *124*, 10596–10604.
41. Joshi, G. K.; Blodgett, K. N.; Muhoferac, B. B.; Johnson, M. A.; Smith, K. A.; Sardar, R. Ultrasensitive Photoreversible Molecular Sensors of Azobenzene-Functionalized Plasmonic Nanoantennas. *Nano Lett.* **2014**, *14*, 532–540.
42. Mock, J. J.; Smith, D. R.; Schultz, S. Local Refractive Index Dependence of Plasmon Resonance Spectra from Individual Nanoparticles. *Nano Lett.* **2003**, *3*, 485–491.
43. Anker, J. N.; Hall, W. P.; Lyandres, O.; Shah, N. C.; Zhao, J.; Van Duyne, R. P. Biosensing with plasmonic nanosensors. *Nat. Mater.* **2008**, *7*, 442–453.
44. Jain, P. K.; Huang, X.; El-Sayed, I. H.; El-Sayed, M. A. Noble Metals on the Nanoscale: Optical and Photothermal Properties and Some Applications in Imaging, Sensing, Biology, and Medicine. *Acc. Chem. Res.* **2008**, *41*, 1578–1586.
45. Joshi, G. K.; Deitz-McElyea, S.; Johnson, M.; Mali, S.; Korc, M.; Sardar, R. Highly Specific Plasmonic Biosensors for Ultrasensitive MicroRNA Detection in Plasma from Pancreatic Cancer Patients. *Nano Lett.* **2014**, *14*, 6955–6963.
46. Haes, A. J.; Hall, W. P.; Chang, L.; Klein, W. L.; Van Duyne, R. P. A Localized Surface Plasmon Resonance Biosensor: First Steps toward an Assay for Alzheimer's Disease. *Nano Lett.* **2004**, *4*, 1029–1034.
47. Beeram, S. R.; Zamborini, F. P. Purification of Gold Nanoplates Grown Directly on Surfaces for Enhanced Localized Surface Plasmon Resonance Biosensing. *ACS Nano* **2010**, *4*, 3633–3646.
48. Beeram, S. R.; Zamborini, F. P. Selective Attachment of Antibodies to the Edges of Gold Nanostructures for Enhanced Localized Surface Plasmon Resonance Biosensing. *J. Am. Chem. Soc.* **2009**, *131*, 11689–11691.
49. Banholzer, M. J.; Harris, N.; Millstone, J. E.; Schatz, G. C.; Mirkin, C. A. Abnormally Large Plasmonic Shifts in Silica-Protected Gold Triangular Nanoprisms. *Am. J. Phys. Chem. C* **2010**, *114*, 7521–7526.
50. Haes, A. J.; Zou, S.; Schatz, G. C.; Van Duyne, R. P. Nanoscale Optical Biosensor: Short Range Distance Dependence of the Localized Surface Plasmon Resonance of Noble Metal Nanoparticles. *J. Phys. Chem. B* **2004**, *108*, 6961–6968.
51. Beeram, S. R.; Zamborini, F. P. Effect of Protein Binding Coverage, Location, and Distance on the Localized Surface Plasmon Resonance Response of Purified Au Nanoplates Grown Directly on Surfaces. *J. Phys. Chem. C* **2011**, *115*, 7364–7371.
52. Feuz, L.; Jonsson, M. P.; Höök, F. Material-Selective Surface Chemistry for Nanoplasmatic Sensors: Optimizing Sensitivity and Controlling Binding to Local Hot Spots. *Nano Lett.* **2012**, *12*, 873–879.
53. Dong, H.; Zhang, J.; Ju, H.; Lu, H.; Wang, S.; Jin, S.; Hao, K.; Du, H.; Zhang, X. Highly Sensitive Multiple microRNA Detection Based on Fluorescence Quenching of Graphene Oxide and Isothermal Strand-Displacement Polymerase Reaction. *Anal. Chem.* **2012**, *84*, 4587–4593.
54. Harmsen, S.; Huang, R.; Wall, M. A.; Karabeber, H.; Samii, J. M.; Spalvieri, M.; White, J. R.; Monette, S.; O'Connor, R.; Pitter, K. L.; et al. Surface-enhanced resonance Raman scattering nanostars for high-precision cancer imaging. *Sci. Transl. Med.* **2015**, *7*, 271ra7.
55. Marinakos, S. M.; Chen, S.; Chilkoti, A. Plasmonic Detection of a Model Analyte in Serum by a Gold Nanorod Sensor. *Anal. Chem.* **2007**, *79*, 5278–5283.
56. Elhadj, S.; Singh, G.; Saraf, R. F. Optical Properties of an Immobilized DNA Monolayer from 255 to 700 nm. *Langmuir* **2004**, *20*, 5539–5543.
57. Hao, E.; Schatz, G. C. Electromagnetic fields around silver nanoparticles and dimers. Electromagnetic fields around silver nanoparticles and dimers. *J. Chem. Phys.* **2004**, *120*, 357–366.
58. Sherry, L. J.; Chang, S.-H.; Schatz, G. C.; Van Duyne, R. P.; Wiley, B. J.; Xia, Y. Localized Surface Plasmon Resonance Spectroscopy of Single Silver Nanocubes. *Nano Lett.* **2005**, *5*, 2034–2038.
59. Joshi, G. K.; McClory, P. J.; Muhoferac, B. B.; Kumbhar, A.; Smith, K. A.; Sardar, R. Designing Efficient Localized Surface Plasmon Resonance-Based Sensing Platforms: Optimization of Sensor Response by Controlling the Edge Length of Gold Nanoprisms. *J. Phys. Chem. C* **2012**, *116*, 20990–21000.
60. Hihath, J.; Xu, B.; Zhang, P.; Tao, N. Study of single-nucleotide polymorphisms by means of electrical conductance measurements. *Proc. Natl. Acad. Sci. U. S. A.* **2005**, *102*, 16979–16983.
61. Kelley, S. O.; Barton, J. K. Electron Transfer Between Bases in Double Helical DNA. Electron Transfer Between Bases in Double Helical DNA. *Science* **1999**, *283*, 375–381.
62. Murphy, C. J.; Arkin, M. R.; Jenkins, Y.; Ghatlia, N. D.; Bossmann, S. H.; Turro, N. J.; Barton, J. K. Long-range photoinduced electron transfer through a DNA helix. *Science* **1993**, *262*, 1025–1029.
63. Renaud, N.; Berlin, Y. A.; Ratner, M. A. Impact of a single base pair substitution on the charge transfer rate along short DNA hairpins. *Proc. Natl. Acad. Sci. U. S. A.* **2013**, *110*, 14867–14871.
64. Cisse, I. I.; Kim, H.; Ha, T. A rule of seven in Watson-Crick base-pairing of mismatched sequences. *Nat. Struct. Mol. Biol.* **2012**, *19*, 623–627.
65. Setoyama, T.; Zhang, X.; Natsugoe, S.; Calin, G. A. microRNA-10b: A New Marker or the Marker of Pancreatic Ductal Adenocarcinoma? *Clin. Cancer Res.* **2011**, *17*, 5527–5529.
66. du Rieu, M. I. C.; Torrisani, J. r. m.; Selves, J.; Al Saati, T.; Souque, A.; Dufresne, M. n.; Tsongalis, G. J.; Suriawinata, A. A.; Carrere, N.; Buscail, L.; et al. MicroRNA-21 Is Induced Early in Pancreatic Ductal Adenocarcinoma Precursor Lesions. *Clin. Chem.* **2010**, *56*, 603–612.

67. Szafranska, A. E.; Doleshal, M.; Edmunds, H. S.; Gordon, S.; Luttges, J.; Munding, J. B.; Barth, R. J.; Gutmann, E. J.; Suriawinata, A. A.; Marc Pipas, J.; et al. Analysis of MicroRNAs in Pancreatic Fine-Needle Aspirates Can Classify Benign and Malignant Tissues. *Clin. Chem.* **2008**, *54*, 1716–1724.
68. Lee, E. J.; Gusev, Y.; Jiang, J.; Nuovo, G. J.; Lerner, M. R.; Frankel, W. L.; Morgan, D. L.; Postier, R. G.; Brackett, D. J.; Schmittgen, T. D. Expression profiling identifies microRNA signature in pancreatic cancer. *Int. J. Cancer* **2007**, *120*, 1046–1054.
69. Ouyang, H.; Gore, J.; Deitz, S.; Korc, M. microRNA-10b enhances pancreatic cancer cell invasion by suppressing TIP30 expression and promoting EGF and TGF-[beta] actions. *Oncogene* **2014**, *33*, 4664–4674.
70. Melo, S. A.; Luecke, L. B.; Kahlert, C.; Fernandez, A. F.; Gammon, S. T.; Kaye, J.; LeBleu, V. S.; Mittendorf, E. A.; Weitz, J.; Rahbari, N.; et al. Glypican-1 identifies cancer exosomes and detects early pancreatic cancer. *Nature* **2015**, *523*, 177–182.
71. Ide, T.; Kitajima, Y.; Miyoshi, A.; Ohtsuka, T.; Mitsuno, M.; Ohtaka, K.; Miyazaki, K. The Hypoxic Environment in Tumor-Stromal Cells Accelerates Pancreatic Cancer Progression via the Activation of Paracrine Hepatocyte Growth Factor/c-Met Signaling. *Ann. Surg. Oncol.* **2007**, *14*, 2600–2607.
72. Chang, Q.; Jurisica, I.; Do, T.; Hedley, D. W. Hypoxia Predicts Aggressive Growth and Spontaneous Metastasis Formation from Orthotopically Grown Primary Xenografts of Human Pancreatic Cancer. *Cancer Res.* **2011**, *71*, 3110–3120.
73. Turchinovich, A.; Weiz, L.; Langheinz, A.; Burwinkel, B. Characterization of extracellular circulating microRNA. Characterization of extracellular circulating microRNA. *Nucleic Acids Res.* **2011**, *39*, 7223–7233.
74. Arroyo, J. D.; Chevillet, J. R.; Kroh, E. M.; Ruf, I. K.; Pritchard, C. C.; Gibson, D. F.; Mitchell, P. S.; Bennett, C. F.; Pogosova-Agadjanyan, E. L.; Stirewalt, D. L.; et al. Argonaute2 complexes carry a population of circulating microRNAs independent of vesicles in human plasma. *Proc. Natl. Acad. Sci. U. S. A.* **2011**, *108*, 5003–5008.
75. Ni, X. G.; Bai, X. F.; Mao, Y. L.; Shao, Y. F.; Wu, J. X.; Shan, Y.; Wang, C. F.; Wang, J.; Tian, Y. T.; Liu, Q.; et al. The clinical value of serum CEA, CA19–9, and CA242 in the diagnosis and prognosis of pancreatic cancer. *Eur. J. Surg. Oncol.* **2005**, *31*, 164–169.
76. DiMagno, M. J.; DiMagno, E. P. Chronic pancreatitis. Chronic pancreatitis. *Curr. Opin. Gastroenterol.* **2012**, *28*, 523–531.
77. Lowenfels, A. B.; Maisonneuve, P.; Cavallini, G.; Ammann, R. W.; Lankisch, P. G.; Andersen, J. R.; Dimagno, E. P.; Andren-Sandberg, A.; Domellof, L. Pancreatitis and the Risk of Pancreatic Cancer. *N. Engl. J. Med.* **1993**, *328*, 1433–1437.
78. Lawrence, K. N.; Johnson, M. A.; Dolai, S.; Kumbhar, A.; Sardar, R. Solvent-like ligand-coated ultrasmall cadmium selenide nanocrystals: strong electronic coupling in a self-organized assembly. *Nanoscale* **2015**, *7*, 11667–11677.
79. Joshi, G. K.; Smith, K. A.; Johnson, M. A.; Sardar, R. Temperature-Controlled Reversible Localized Surface Plasmon Resonance Response of Polymer-Functionalized Gold Nanoprisms in the Solid State. *J. Phys. Chem. C* **2013**, *117*, 26228–26237.
80. Liu, F.; Korc, M. Cdk4/6 Inhibition Induces Epithelial–Mesenchymal Transition and Enhances Invasiveness in Pancreatic Cancer Cells. *Mol. Cancer Ther.* **2012**, *11*, 2138–2148.